Supplementary Information for

Monitoring Spatially Heterogeneous Subsidence of Transportation Infrastructure in Beijing Using Sentinel-1 InSAR Time Series

Weizhen Lin [1,2], Xi Guo[1], Yidi Wang[1,2], Changyang Hu[1,2] and Zhang Yunjun [1,2,*]

[1] National Key Laboratory of Microwave Imaging, Aerospace Information Research Institute, Chinese Academy of Sciences, Beijing 100190, China; linweizhen23@mails.ucas.ac.cn (W.L.); guoxi@aircas.ac.cn (X.G.); wangyidi23@mails.ucas.ac.cn (Y.W.); huchangyang24@mails.ucas.ac.cn (C.H.)

[2] School of Electronic, Electrical and Communication Engineering, University of Chinese Academy of Sciences, Beijing 100049, China

* Correspondence: yunjunz@aircas.ac.cn

Contents of this file

Table S1. ISCE2 parameter file used for Sentinel-1 processing.

Table S2. MintPy configuration file used for time-series analysis.

Figure S1. Perpendicular baseline history for Sentinel-1 ascending and descending tracks.

Figure S2. Interferogram network for ascending and descending tracks.

Figure S3. Coherence history for Sentinel-1 acquisitions.

Figure S4. Temporal and average spatial coherence maps for ascending and descending tracks.

Figure S5. Triplet-closure validation for ascending and descending interferograms.

Figure S6. Comparison of tropospheric delay fields derived from ERA5 and GACOS

Figure S7. LOS displacement time-series for ascending track A142.

Figure S8. LOS displacement time-series for descending track D47.

Figure S9. Cumulative subsidence and gradient profiles along Beijing Ring Roads.

Figure S10. Cumulative subsidence and gradient profiles along major expressways.

Figure S11. Cumulative subsidence and gradient profiles along BCIA and BDIA runways.

Figure S12. Comparison between InSAR-derived line-of-sight (LOS) deformation and groundwater-level variations at four monitoring wells

Table S1. ISCE2 parameter file used for Sentinel-1 topsStack processing

Parameter	Value
processor	auto
workflow	interferogram
demSNWE	auto
demFile	auto
demSource	srtm1
demFillValue	0
demUrl	none
demBuffer	3
boundingBox	39.40,40.363,116.00,116.79
referenceDate	20150730
rangeLooks	9
filtStrength	0.7
unwrapMethod	snaphu
useGPU	yes
numProcess	48
virtualMerge	no
coregistration	geometry
swathNum	auto
numConnection	5
orbitDir	~/beijing/S1_A142/orbits
auxDir	/home/linwz/data/aux/
startDate	none
endDate	none

Table S2. MintPy configuration file used for time-series analysis.

	A142	**D47**
Parameter	Value	Value
reference.lalo	39.904,116.394	39.904,116.394
subset.lalo	39.41,40.36,116.01,116.74	39.41,40.36,116.01,116.74
network.coherenceBased	yes	yes
network.minCoherence	0.55	0.55
network.excludeDate	20150730,20160630,20160724,20170625,20211107,20220611,20220623,20220705	None
unwrapError.method	bridging	bridging
unwrapError.bridgePtsRadius	auto	auto
networkInversion.weightFunc	auto	auto
solidEarthTides	yes	yes
ionosphericDelay.method	auto	auto
troposphericDelay.method	pyaps	pyaps

troposphericDelay.weatherModel	ERA5	ERA5
topographicResidual	yes	yes
geocode	yes	yes

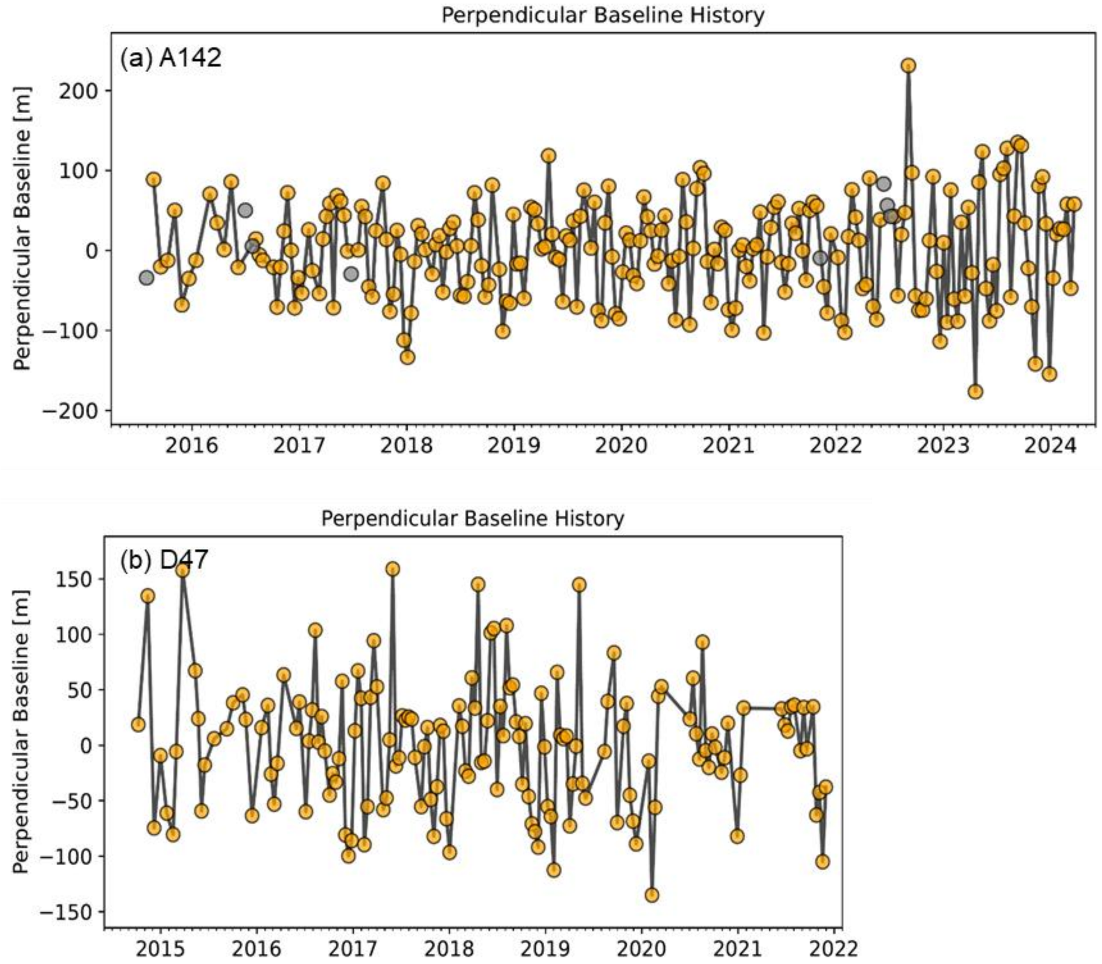

Figure S1. Perpendicular baseline history for Sentinel-1 acquisitions. (a) Ascending track A142 (2016–2024) shows generally stable perpendicular baselines, with most values falling within ±150 m. Although occasional larger baselines appear, the overall geometry remains consistent and suitable for reliable interferogram generation. (b) Descending track D47 (2015–2022) exhibits a similar baseline pattern, with the majority of baselines also within ±150 m. The stable perpendicular baseline distribution supports robust interferometric processing for the descending dataset.

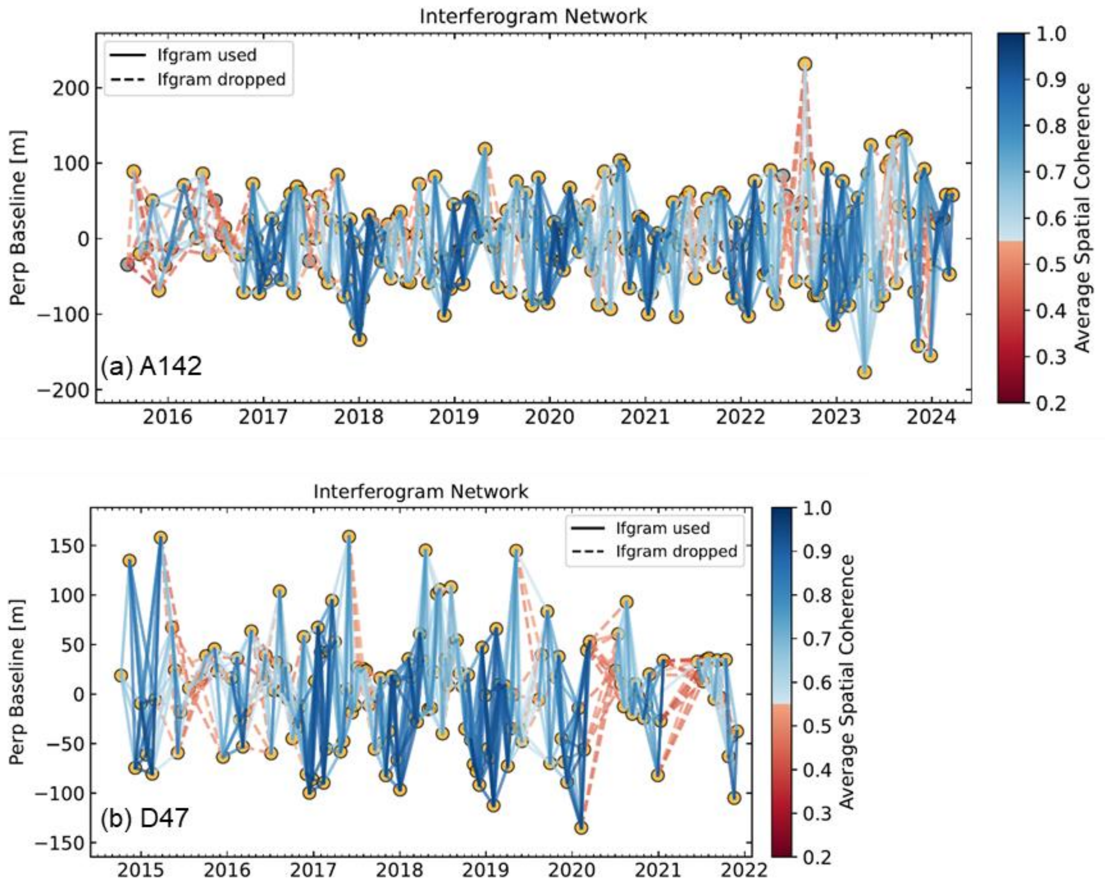

Figure S2. Interferogram network for Sentinel-1 acquisitions. Figure S2. Interferogram network for Sentinel-1 acquisitions. (a) Ascending track A142 and (b) descending track D47. Solid blue lines represent interferograms retained for SBAS processing, while dashed red lines denote interferograms discarded based on the coherence threshold. Line color indicates the average spatial coherence, illustrating the temporal and geometric distribution of interferogram quality across the dataset.

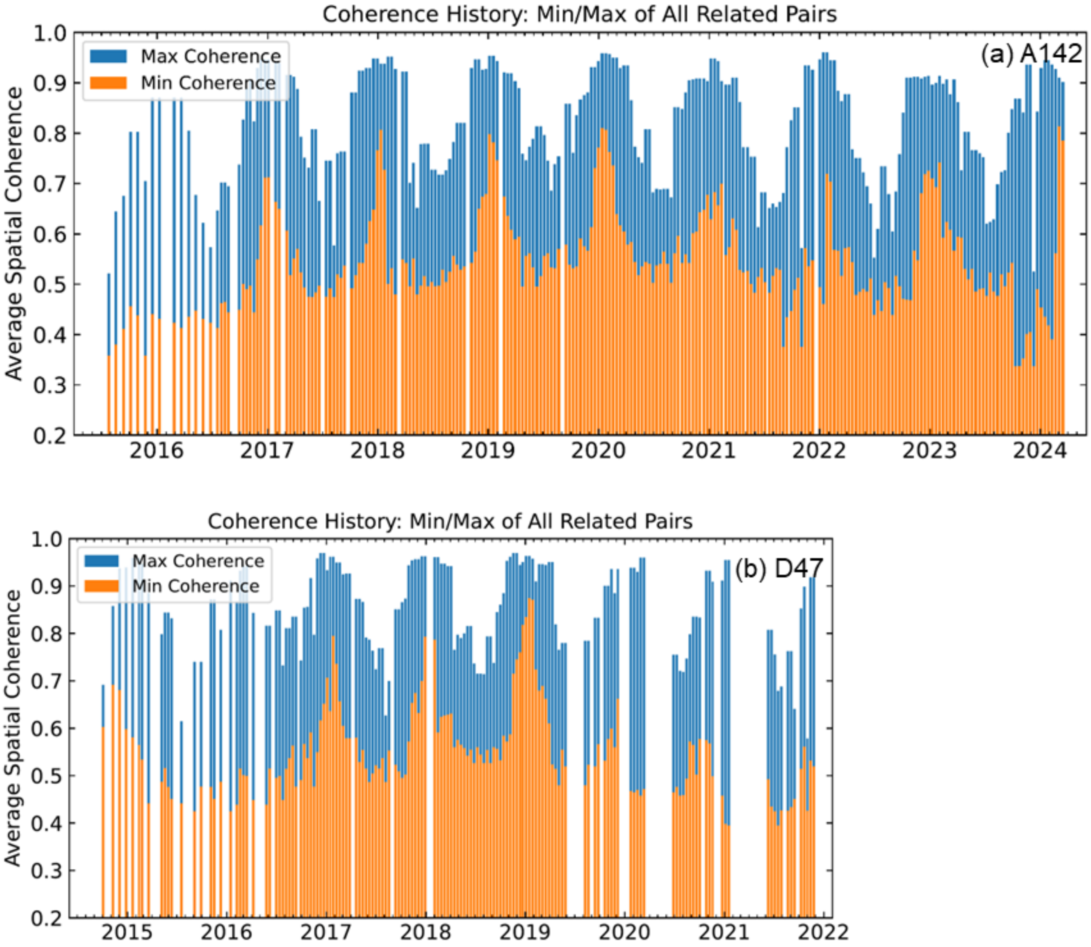

Figure S3. Coherence history for Sentinel-1 acquisitions.(a) Ascending track A142 and (b) descending track D47. The plots show the minimum and maximum average spatial coherence among all interferogram pairs at each acquisition time. Both tracks maintain generally stable and sufficiently high coherence throughout their observation periods, indicating consistently good interferometric data quality and supporting the reliability of phase unwrapping and subsequent time-series deformation analysis.

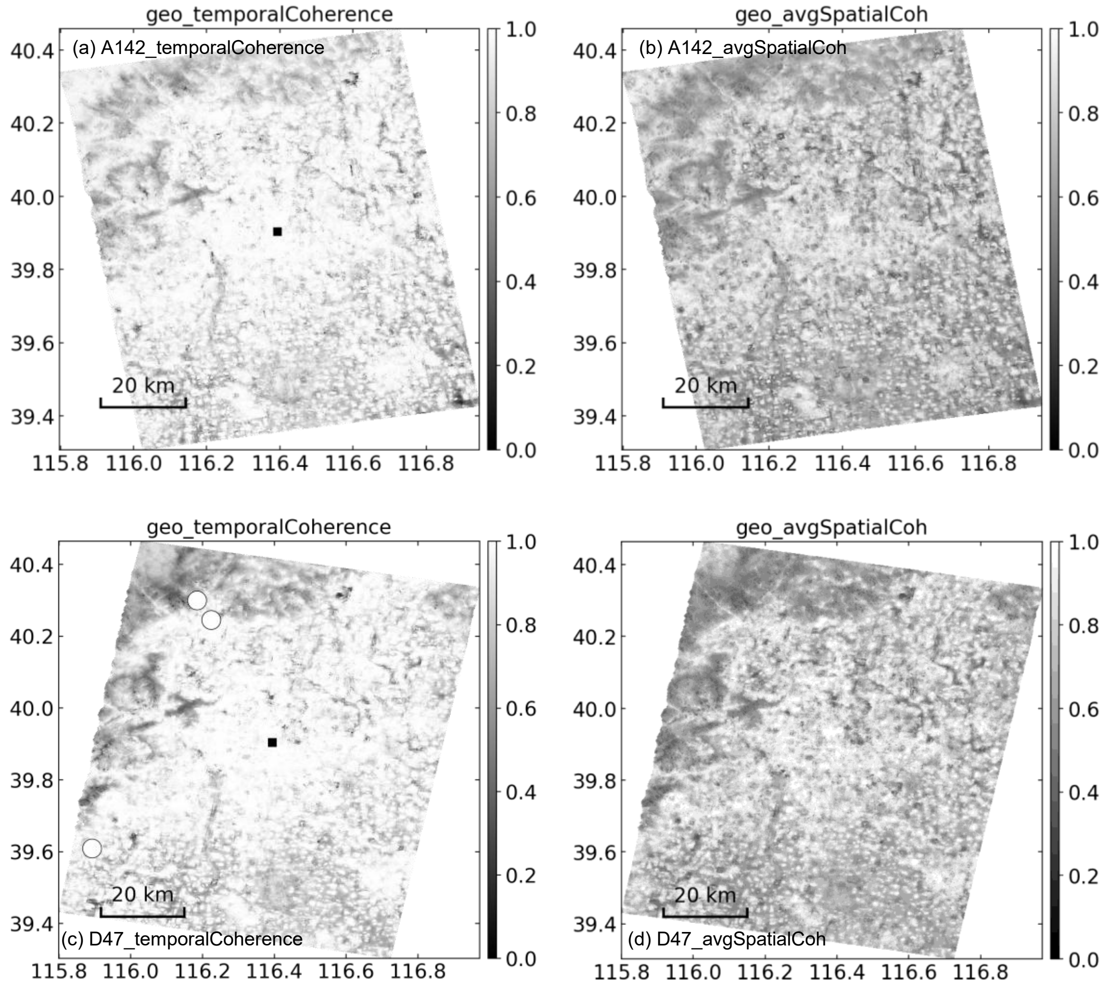

Figure S4. Temporal and average spatial coherence maps for Sentinel-1 acquisitions. **(a)** Temporal coherence and **(b)** average spatial coherence for the ascending track **A142**, and **(c)** temporal coherence and **(d)** average spatial coherence for the descending track **D47**. The maps show the long-term mean coherence computed from all interferogram pairs, revealing the spatial variability of phase stability across the study area. High-coherence regions indicate stable surfaces suitable for reliable time-series inversion, whereas low-coherence areas are primarily associated with decorrelation due to vegetation, land-cover changes, or water bodies.

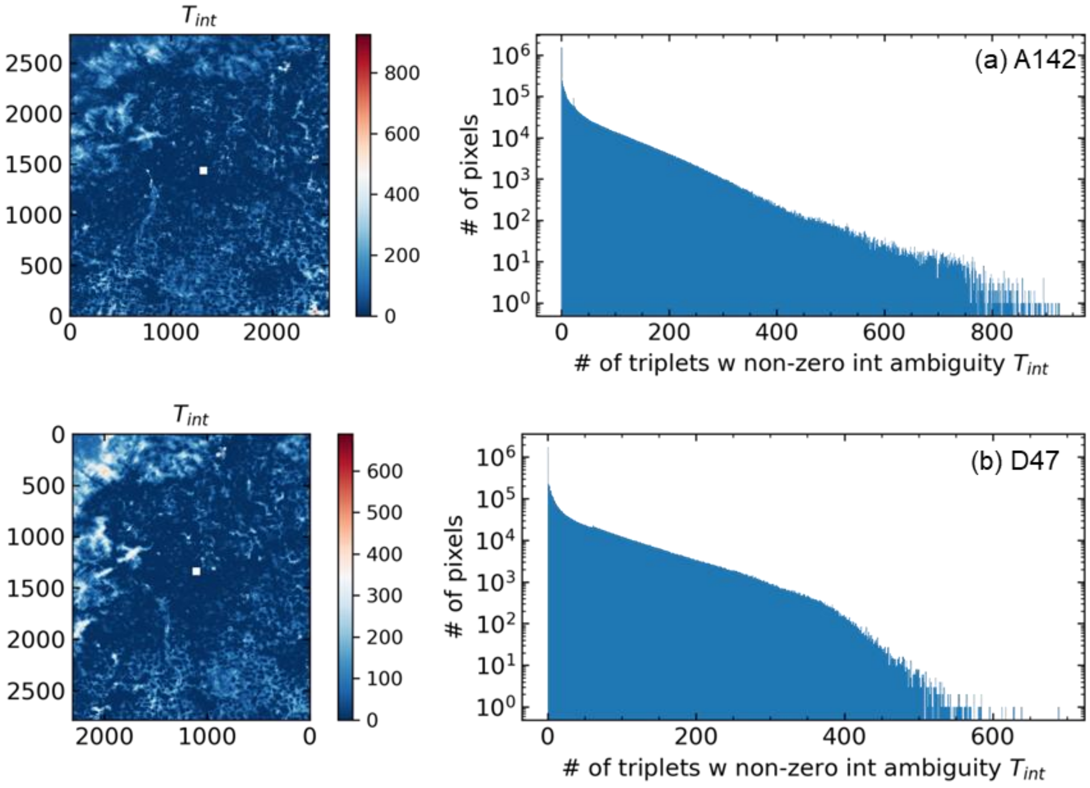

Figure S5. Triplet-closure validation for Sentinel-1 interferograms.(a) Ascending track A142 and (b) descending track D47. The maps show, for each pixel, the number of interferogram triplets exhibiting non-zero integer ambiguities, whereas the accompanying histograms display the frequency distribution of these counts across all coherent pixels. For both tracks, the overwhelming majority of pixels show zero or only a few closure inconsistencies, indicating strong internal phase consistency. The low triplet-closure counts confirm that the unwrapped phases are highly reliable and that no significant unwrapping errors propagate through the interferogram network.

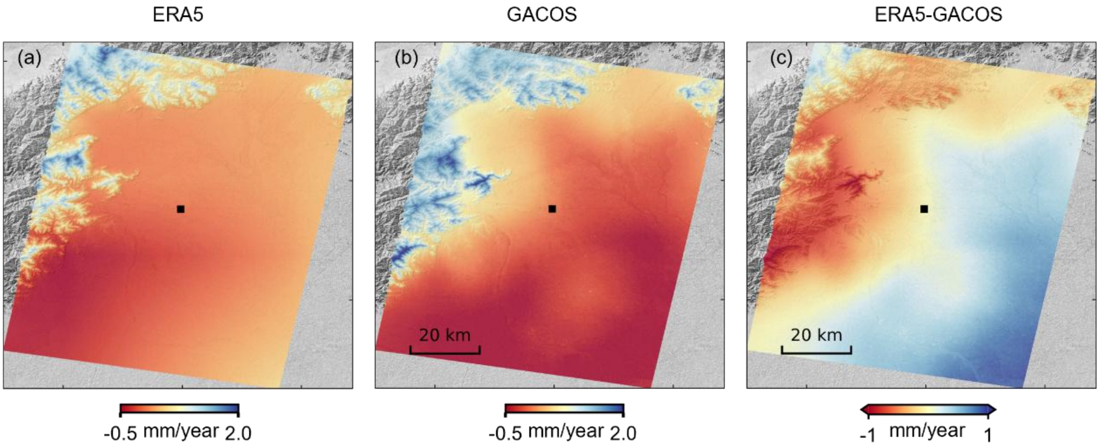

Figure S6. Comparison of tropospheric delay fields derived from ERA5 and GACOS. (a) Tropospheric delay estimated from ERA5. (b) Tropospheric delay estimated from GACOS. (c) Difference between ERA5- and GACOS-derived delays (ERA5 – GACOS).Comparison between InSAR-derived line-of-sight (LOS) deformation and groundwater-level variations at four monitoring wells

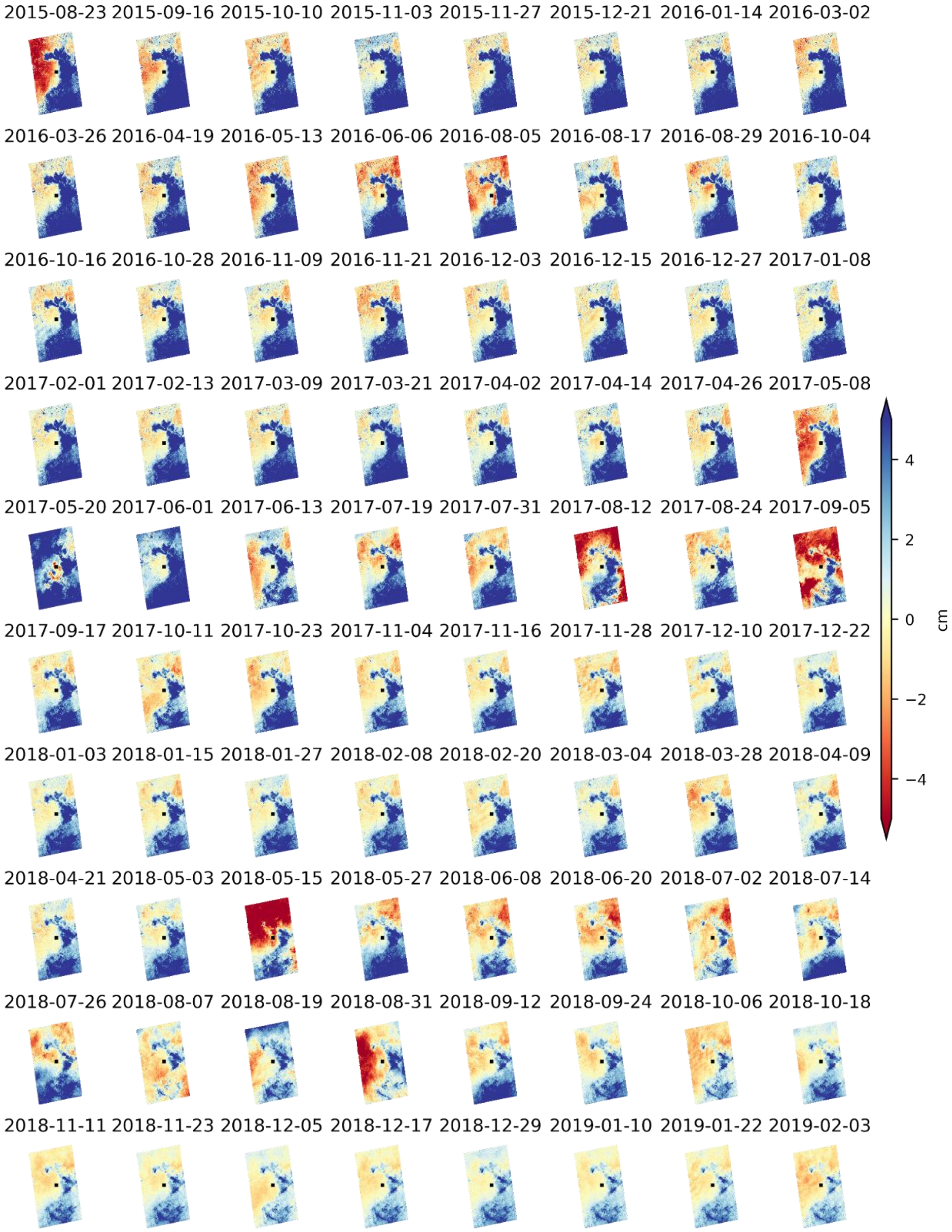

(continued on next page)

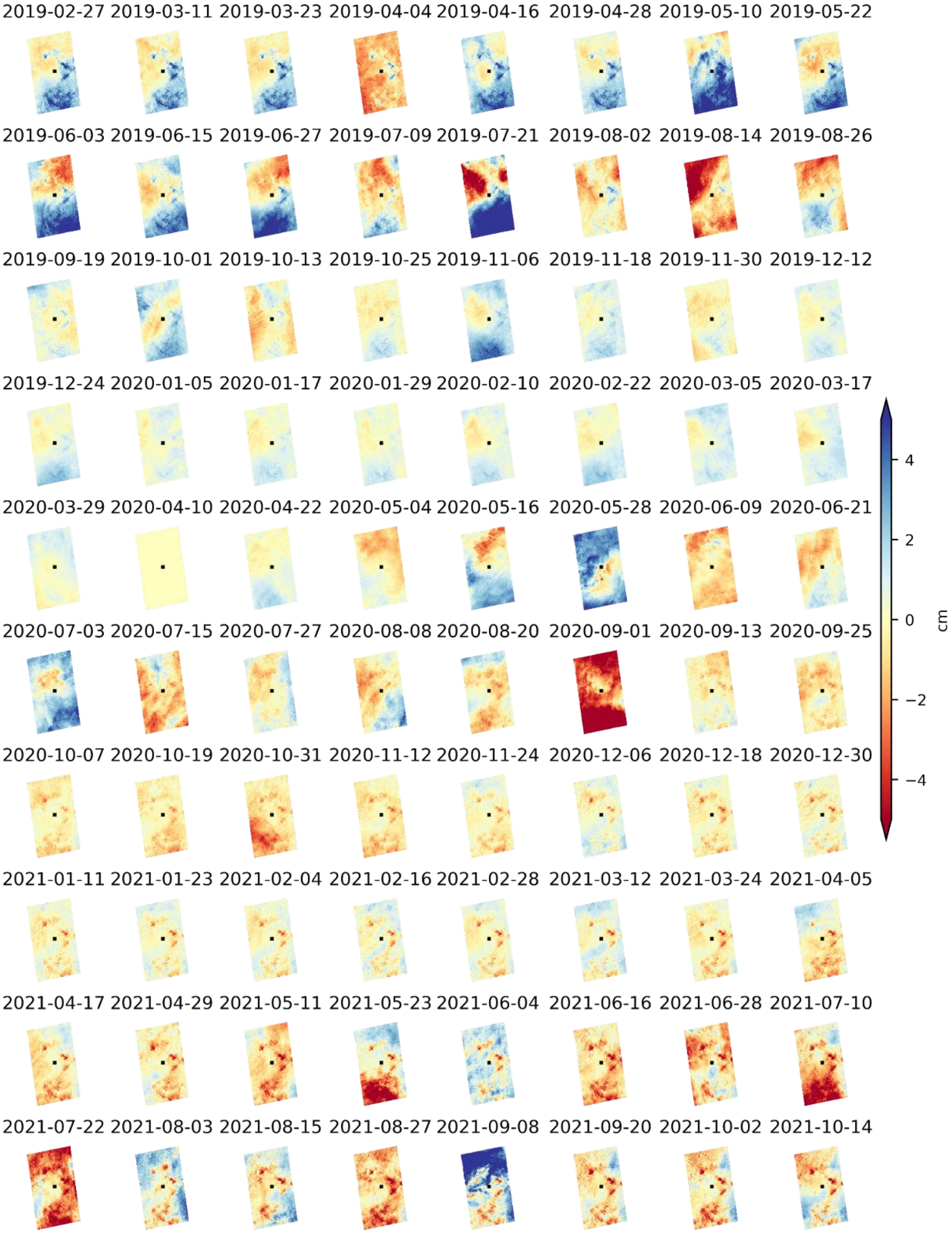

(continued on next page)

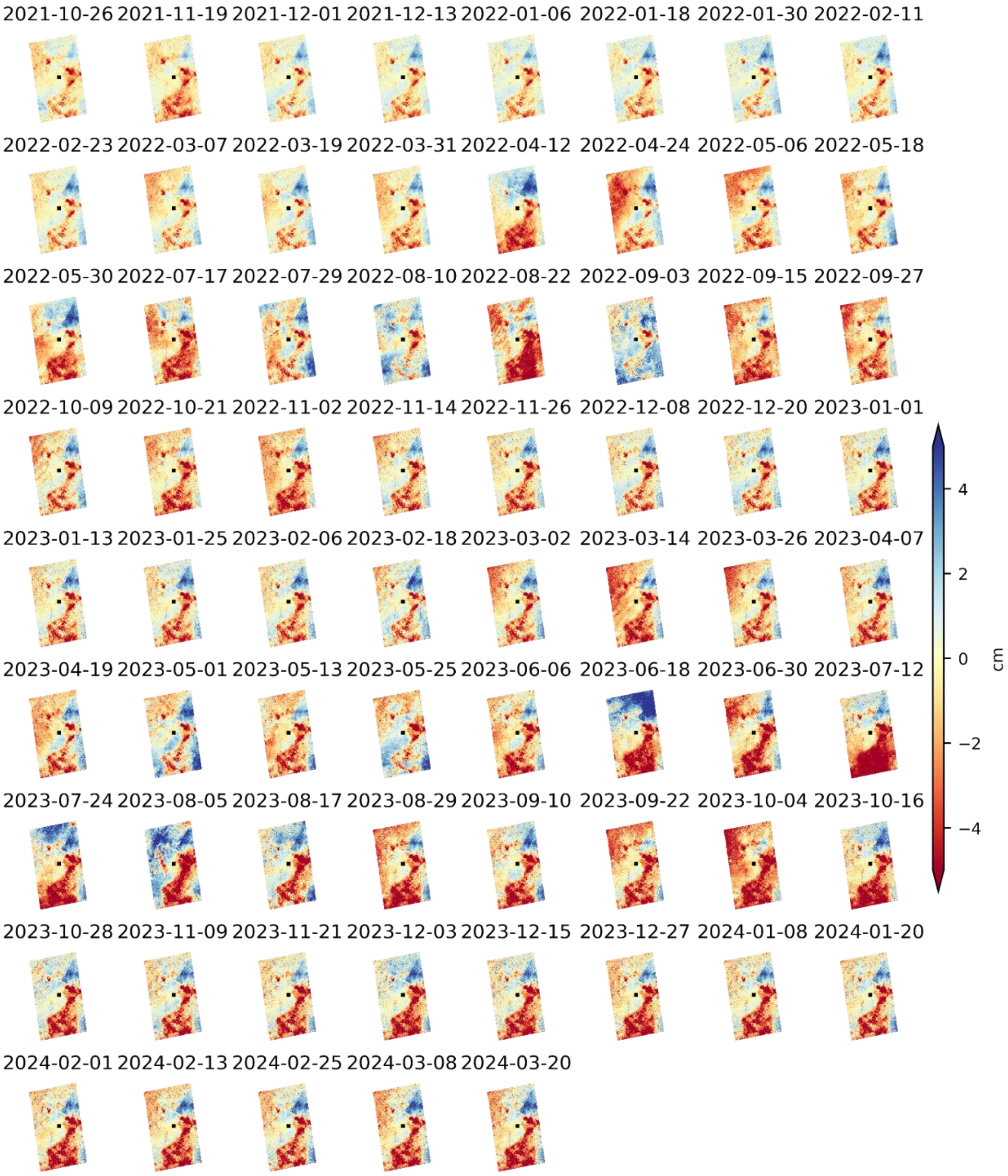

Figure S7. LOS displacement time-series of the Beijing plain from Sentinel-1 ascending track 142. Positive value for motion toward the satellite. Data are wrapped into [-5, 5) cm for display. The time-series has been geocoded, and corrections for error sources, including solid Earth tides, ionospheric and tropospheric delays, and DEM errors, have been applied. Black squares: reference points.

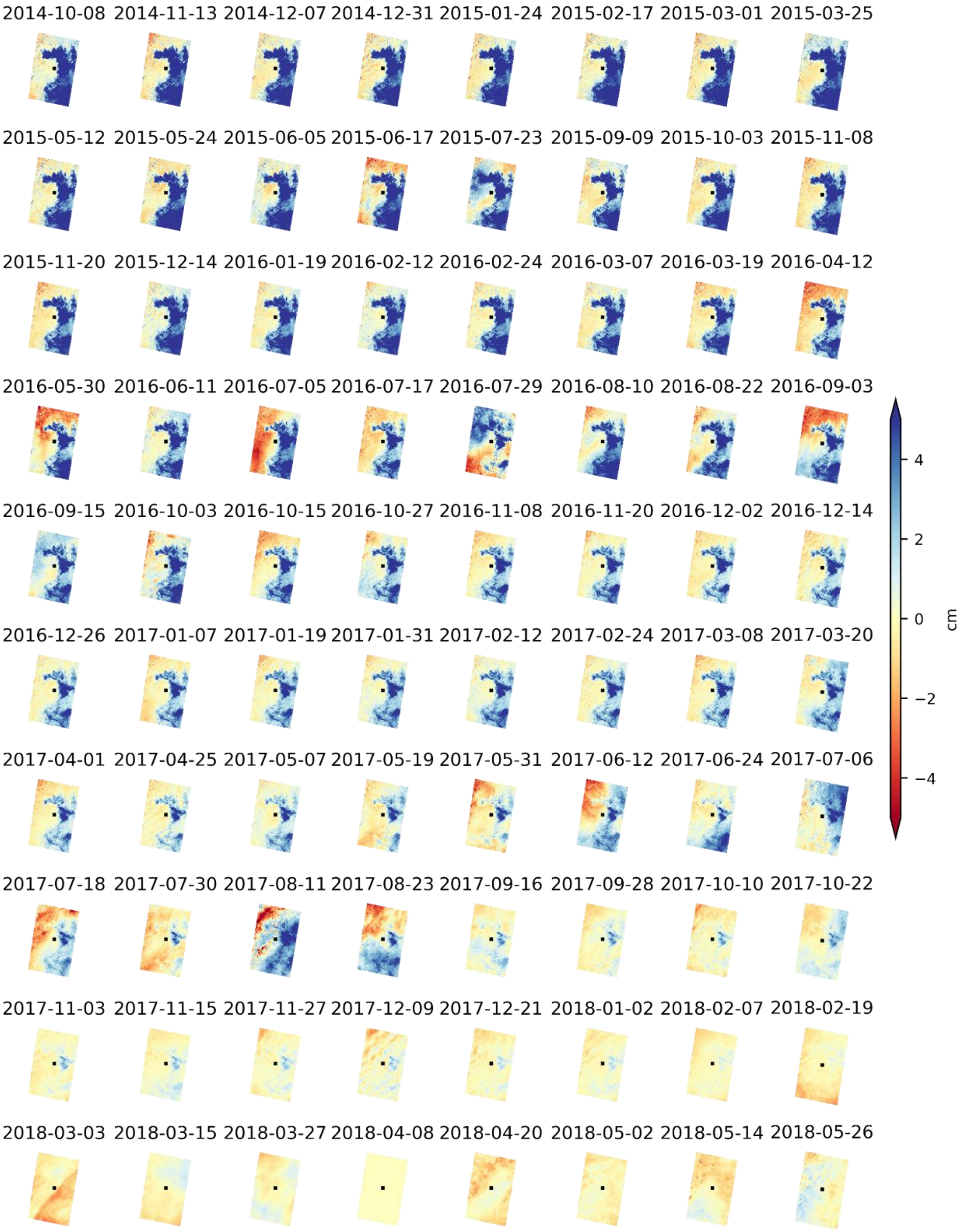

(continued on next page)

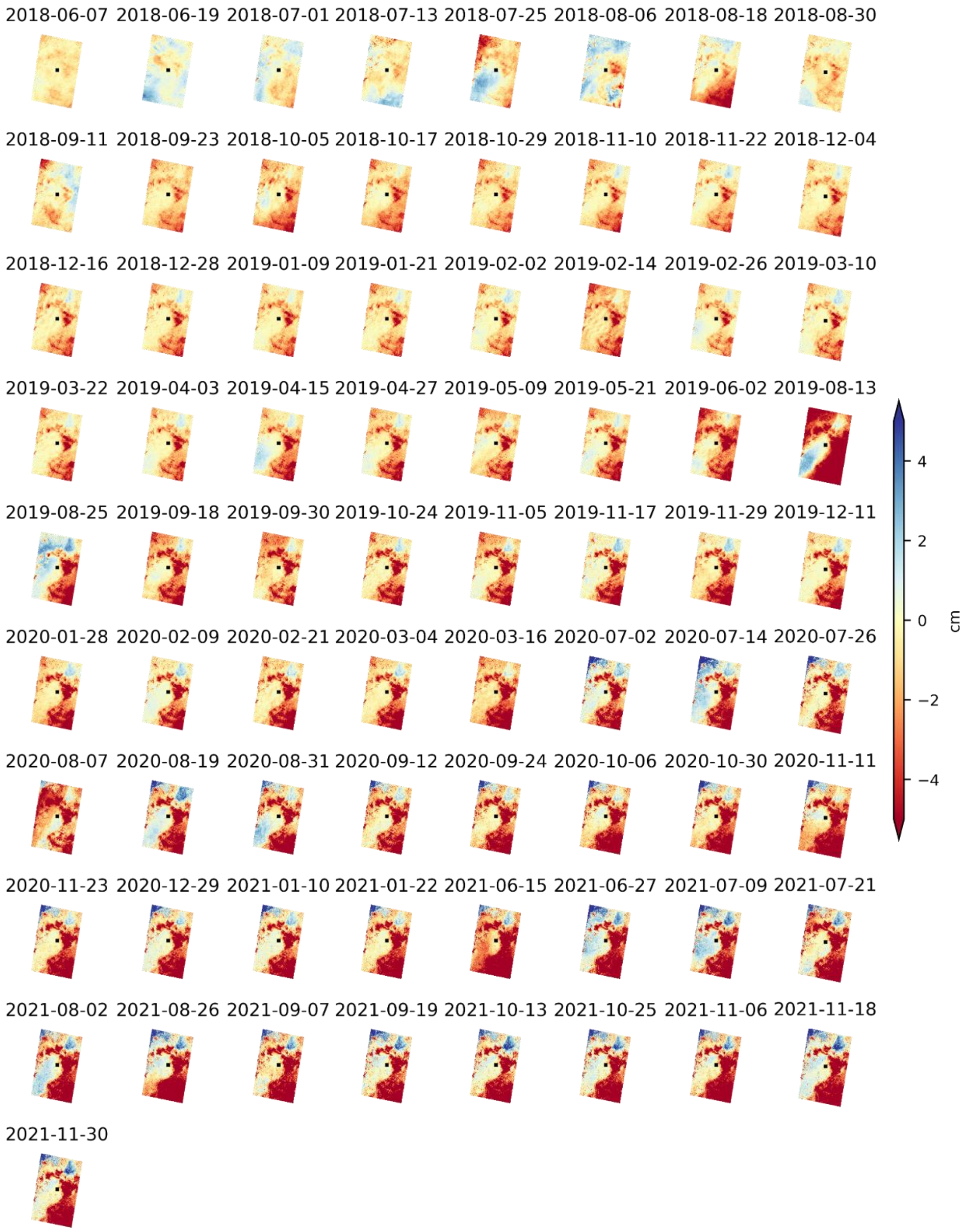

Figure S8. LOS displacement time-series of the Beijing plain from Sentinel-1 descending track 047. Positive value for motion toward the satellite. Data are wrapped into [-5, 5) cm for display. The time-series has been geocoded, and corrections for error sources, including solid Earth tides, ionospheric and tropospheric delays, and DEM errors, have been applied. Black squares: reference points.

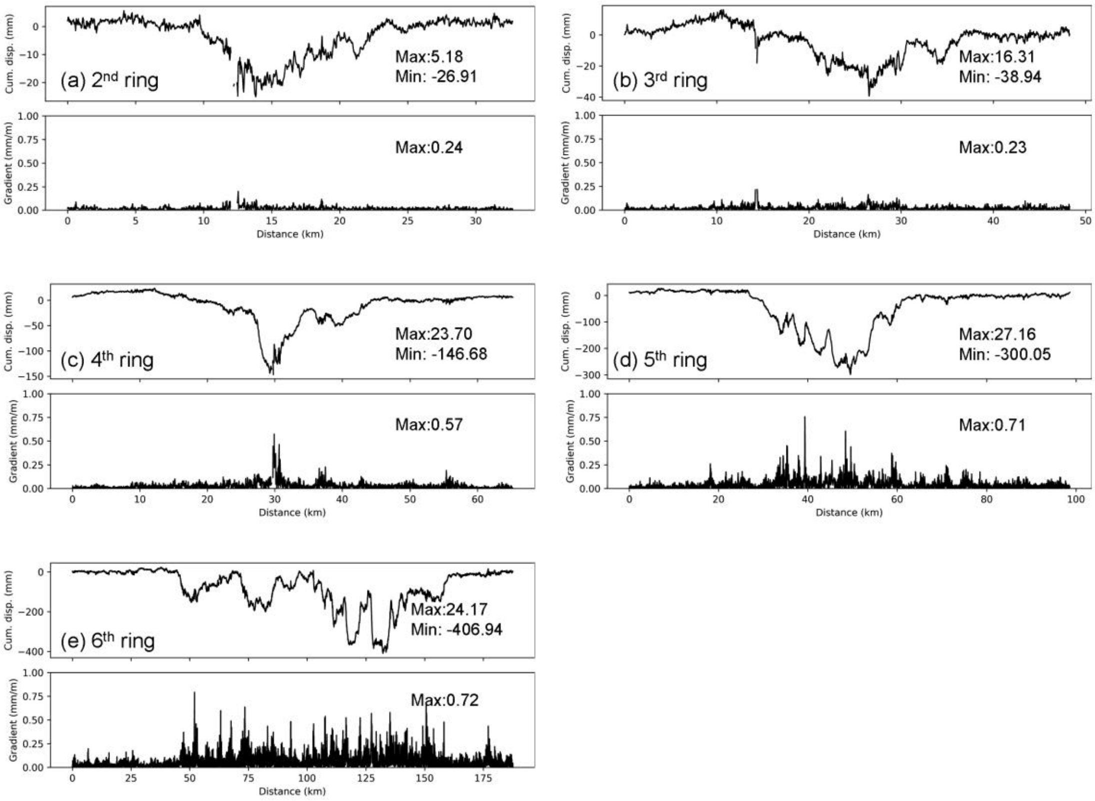

Figure S9. Cumulative subsidence and subsidence gradient profiles along the Beijing Ring Roads. The cumulative displacement curves depict the long-term settlement behavior, while the corresponding gradient profiles highlight zones of localized deformation characterized by rapid spatial changes in displacement. Numerical ranges of cumulative subsidence and maximum gradients are annotated directly in the figure for each Ring Road.

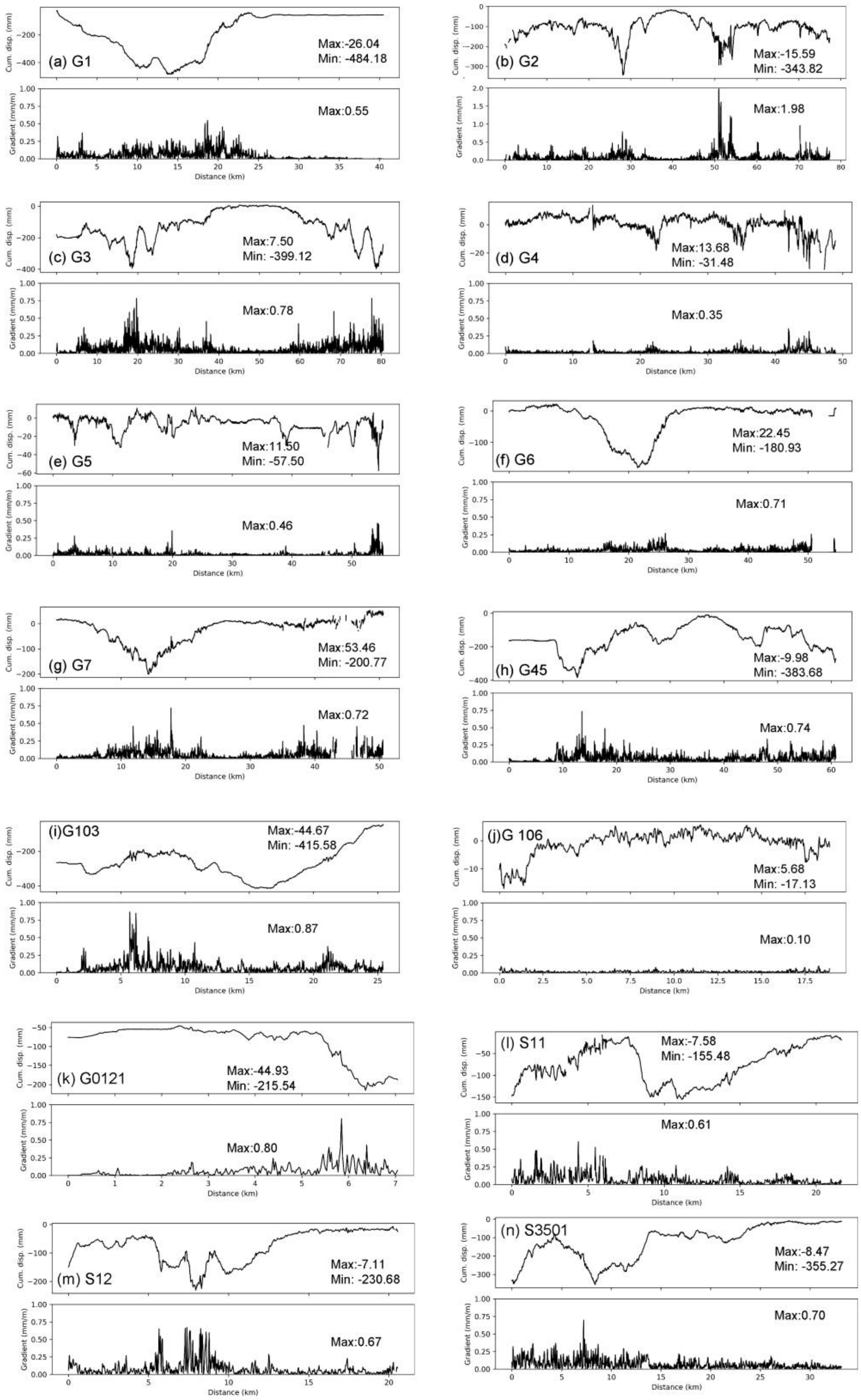

Figure S10. Cumulative subsidence and gradient profiles along major Beijing expressways. The cumulative displacement curves show long-term settlement patterns, and the gradient profiles highlight zones of rapid deformation. Numerical ranges of cumulative subsidence and maximum gradients for each segment are annotated in the figure.

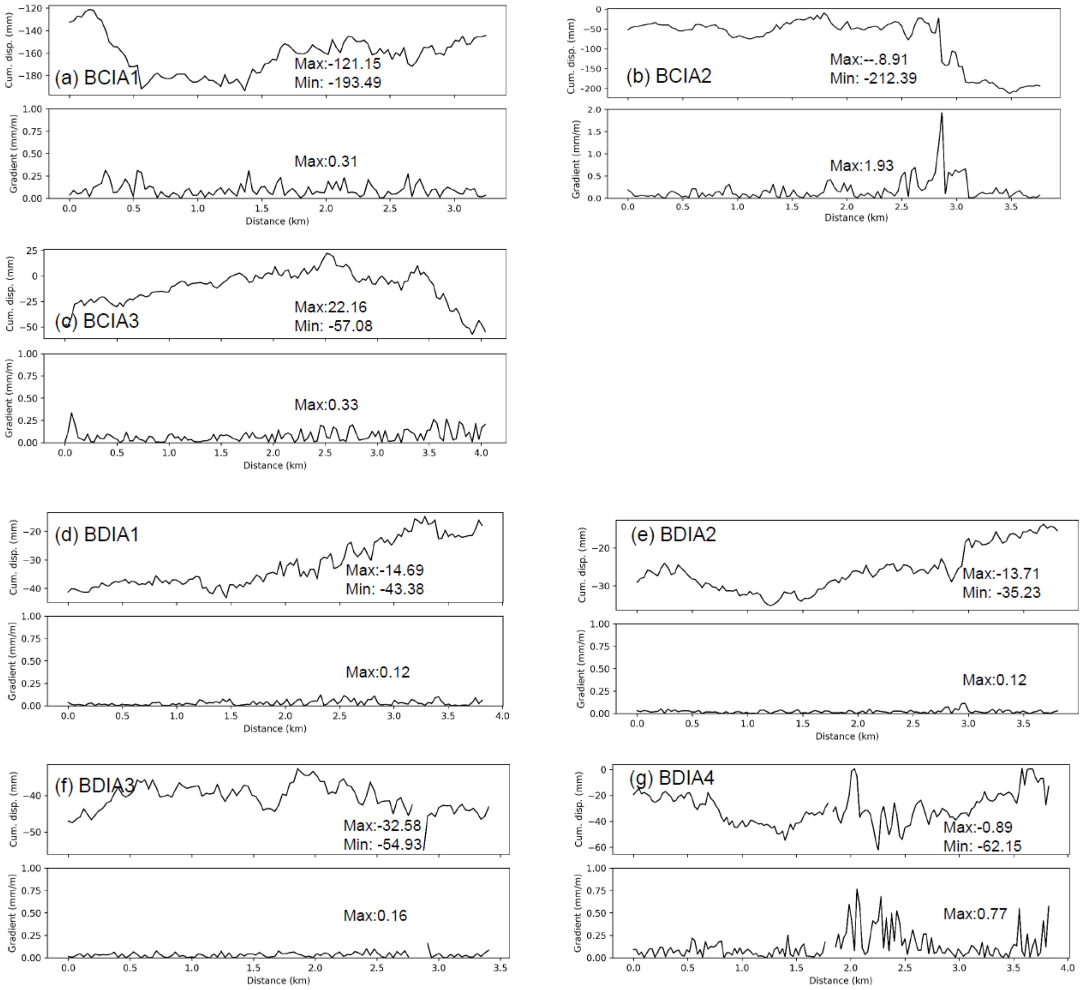

Figure S11. Cumulative subsidence and gradient profiles along the runways of Beijing Capital International Airport (BCIA) and Beijing Daxing International Airport (BDIA) (a–c: BCIA runways; d–g: BDIA runways). The cumulative displacement curves illustrate long-term settlement patterns along each runway segment, while the gradient profiles reveal localized deformation zones with rapid spatial changes in displacement. Numerical ranges of cumulative subsidence and maximum gradients for each runway profile are annotated in the figure.

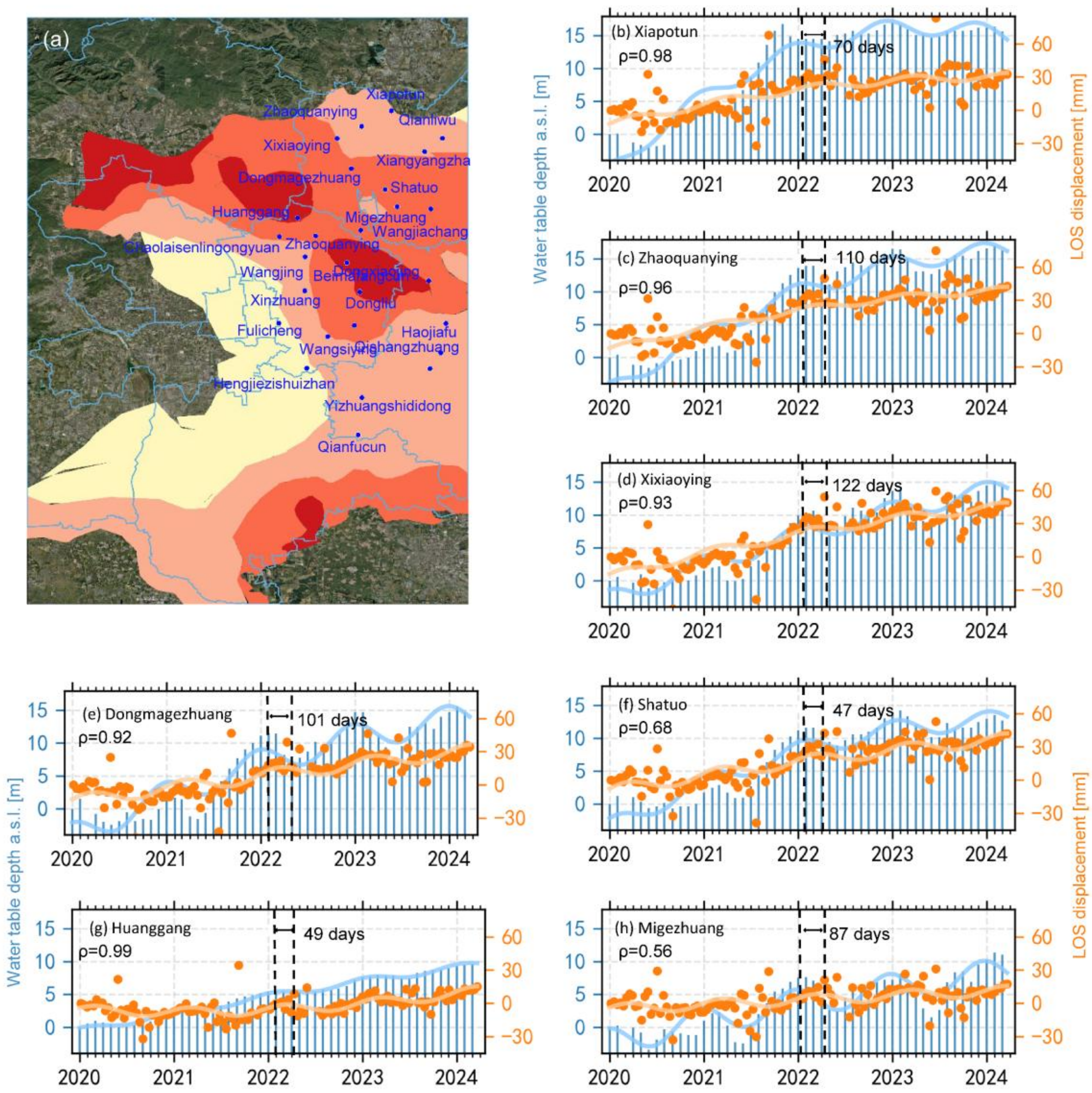

(continued on next page)

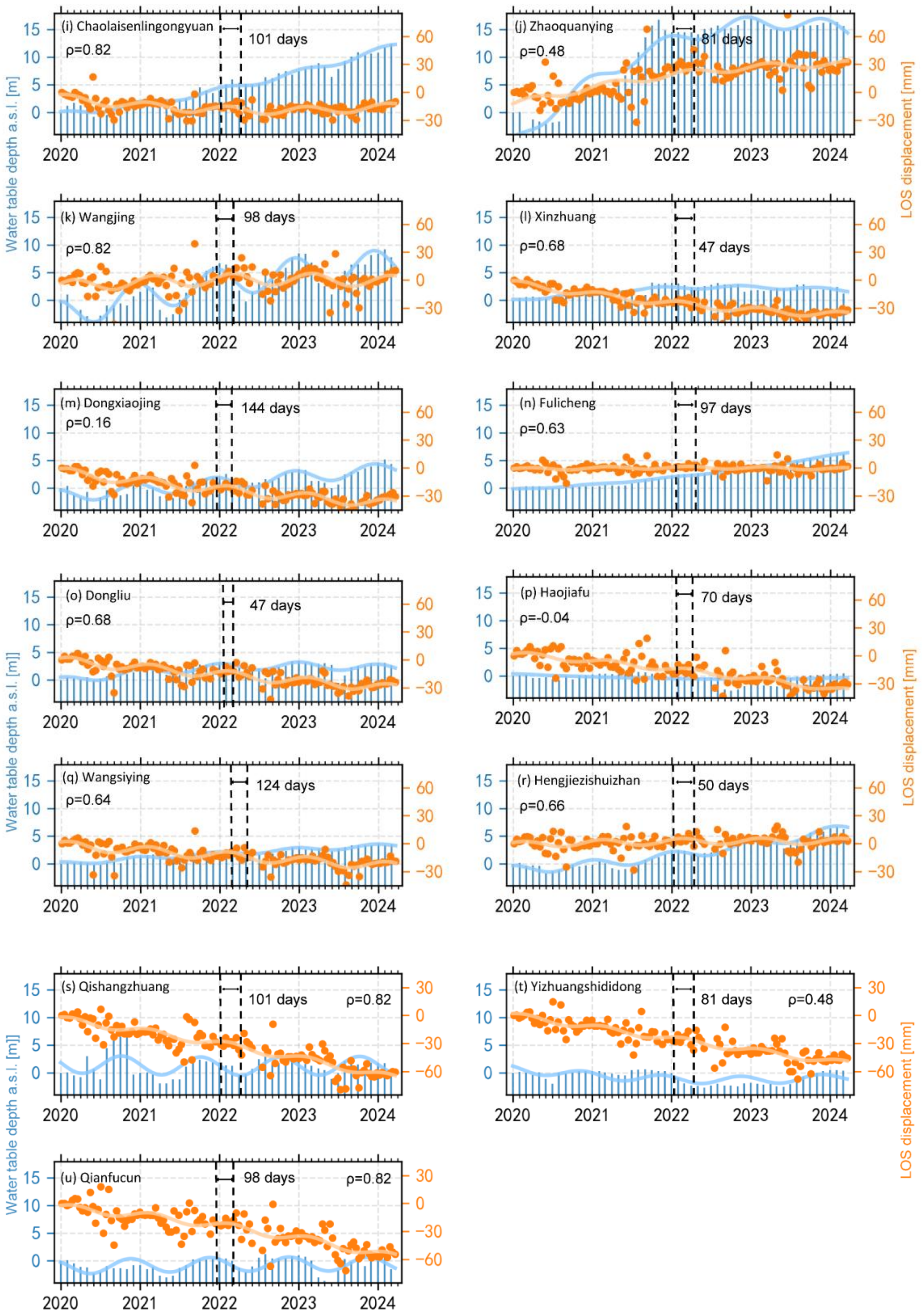

Figure S12. Comparison between InSAR-derived line-of-sight (LOS) deformation and groundwater-level variations at four monitoring wells